Determining ion velocity in the interconnected plume of a cluster of two ECRTs using 2D LIF

IEPC-2024-717

Presented at the 38th International Electric Propulsion Conference, Toulouse, France
June 23-28, 2024

Célian Boyé*, Jaume Navarro-Cavallé† and Mario Merino Martinez‡
Department of Aerospace Engineering, Universidad Carlos III de Madrid, Leganés, Spain

and

Alexis Lecervoisier§ and Stéphane Mazouffre¶
Electric Propulsion team ICARE-CNRS, Orléans, 45071, France

This study presents a detailed investigation into the ion velocity distribution within the interconnected plume of a cluster of two coaxial Electron Cyclotron Resonance Thrusters (ECRTs), in what we denote as a magnetic arch configuration. Two-dimensional Laser-Induced Fluorescence (LIF) spectroscopy and electrostatic probes (Faraday cup, Langmuir probe and retarding potential analyser) are used. Spatially-resolved ion velocity vectors in the transversal plane of the cluster, as well as for a single ECRT, are obtained, with comparable velocity magnitudes ($\sim 6.5\,\mathrm{km/s}$) for both cases. In the case of the single source, the axial component of the velocity increases along the plume expansion. The radial component is null on the source centerline, and increases away from it. For the cluster, a MN-like expansion takes place on the outer side of the sources, while there is partial plasma confinement between the sources. Evidence of two distinct ion populations, coming from the two sources, could not be found. Along the cluster symmetry plane the ion density is $\sim 10^{15}\,\mathrm{m}^{-3}$, whilst the electron temperature drops from $16\,\mathrm{eV}$ to $2\,\mathrm{eV}$. We conclude that the closed-line topology of the magnetic arch topology of the cluster case partially traps ions, resulting in a decrease in terms of v_z along with an increase of radial velocity around the cluster symmetry plane, but this does not prevent the extraction of a free plasma jet.

I. Introduction

EPTs devices group various technologies. Helicon Plasma Thrusters (HPTs)[1–4] and Electron Cyclotron Thrusters (ECRTs)[5–9] remain the main elements of this family. Regarding ECRTs, electrons are heated when the microwave time-varying electric field matches its phase with the gyration of the electrons at the cyclotron resonant frequency given by $\omega_{ce} = eB/m_e$. Once the plasma is generated by collisions between the electrons and the neutral atoms, it is expanded in a magnetic nozzle (MN), radially confined and axially accelerated, generating magnetic thrust by converting electron thermal energy into kinetic ion energy.

A single MN-based EPT has a strong dipole moment, which produces an undesired torque on a spacecraft when it interacts with the planetary B field. Combining two MN-based EPTs with opposing polarities could help with both of these issues. Indeed, two MN-based EPTs assembled side by side have their magnetic field

*PhD Candidate, cboye@ing.uc3m.es.
†Assistant Professor, janavarr@ing.uc3m.es.
‡Associate Professor, marmerin@ing.uc3m.es.
§Electric Propulsion Engineer, Electric Propulsion team ionisation chamberARE-CNRS, alexis.lecervoisier@cnrs-orleans.fr.
¶Research Director, Deputy director of the CNRS ICARE laboratory, stephane.mazouffre@cnrs-orleans.fr.

entangled. Their joined magnetic field forms a magnetic arch (MA) linking one EPT to the other. This new topology exhibits zero net magnetic dipole and can be designed with an overall lower divergence than a single MN. Furthermore, this approach also enables thrust vector control (in the plane of the sources at least) by modifying independently the operation of each source. Clustering also comes with redundancy, as a MN-based EPT can function independently regardless of its assembly in a cluster.

Vereen et al. [10,11] demonstrated experimentally the effect of clustering on two HPTs. A linear superposition of the respective profiles differs from the measurements obtained from a cluster. However, their clustering approach used two same-polarity sources and therefore did not investigate the MA. Both the plasma density and ion exit velocity were shown to increase, resulting in an upgrade in the thruster performance. Merino et al. [12] approached the plasma expansion in the MA configuration with a 2D fluid simulations. The first experimental clustering of ECR sources and the plasma expansion in the MA configuration were done by Boyé et al. [13] Both works concluded that a free plasma jet can be extracted from the MA, albeit at a slightly lower ion energy than a comparable MN.

In the present work we first improve the prototype presented in Boyé et al. [13] to extend its operation time and to perform a more extensive characterisation of the plasma in the MA. Electrostatic probes (a Faraday cup, a Langmuir probe and a retarding potential analyser) are used in a first experimental campaign at Universidad Carlos III de Madrid, providing the ion current density and most probable energy, electron temperature and density, plasma density and the plasma potentials at selected locations. Near-infrared 2D laser-induced Laser-Induced Fluorescence (LIF) is used in a second campaign, held in the ICARE laboratory of the CNRS at Orléans, to determine the spatially-resolved 2D ion velocity vector in the main exhaust plane for both the cluster and a single ECR source.

Section II focuses on the experimental setup. The plume characterisation using electrostatic probes is presented and discussed in Section III. The LIF spectroscopy measurements are reported in Section IV. Subsection IV.A focuses on the axial, radial and total ion velocity maps for a single source, whilst some fluorescence spectra of interest and the axial, radial and total ion velocity maps are presented in Subsection IV.B. Conclusions are finally drawn in Section V.

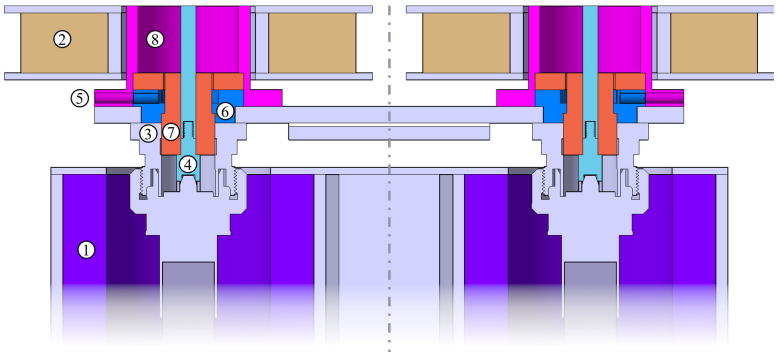

Figure 1. Cross-section top view of the two-ECRT cluster. 1. N42 permanent magnets 2. MN coils 3 . 7-16 DIN receptacle panel 4. Coaxial termination 5. Gas injection 6. Prechamber 7. Ceramics 8. Ionisation chamber.

II. Experimental setup

A. ECR sources

As shown in Figure 1, the cluster is composed of two identical coaxial ECR sources with opposite polarities. Their parallel centerlines are spaced by 120 mm. Their dimensions and characteristics can be found in Table 1. Each source can be decomposed into different sections: a magnetic field generator composed of both permanent magnets and electromagnets, the transmission line (TL) to transmit the power to the ionisation chamber and coaxial termination assembly, and an independent gas injector for each source.

To generate a sufficient high-intensity magnetic field to enable the ECR phenomena, N42 permanent magnets (1) are placed upstream of the source. Additionally, MN coils (2) are responsible for optionally shaping and trimming the magnetic field. Nevertheless, during the experimental campaigns, a constant current of 2 A was used on each coil. Indeed, these electromagnets are subject to heating. Thanks to both the N42 permanent magnets and the MN coils, the 875 G ECR resonance line begins near the ceramic rear plate to spread through the ionisation chamber.

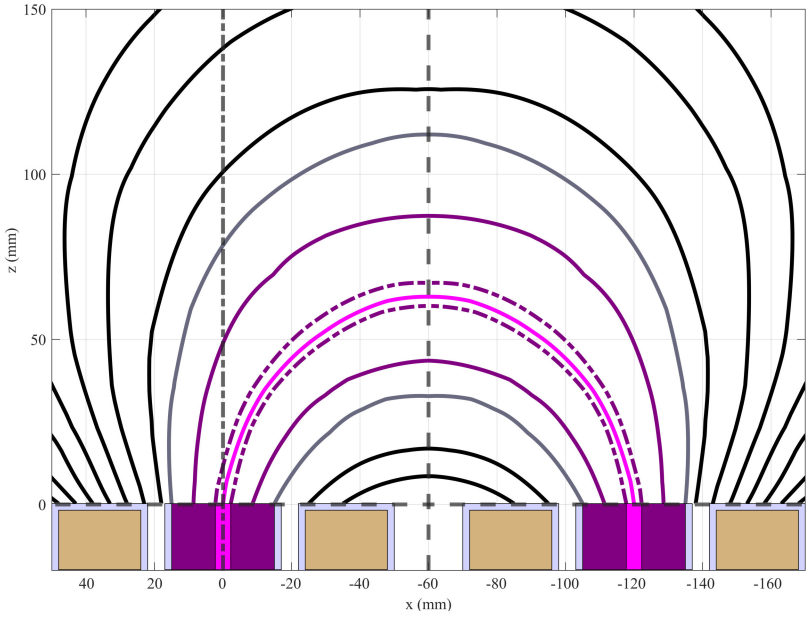

Figure 2. Magnetic field lines of the cluster with $2A$ set on each MN coil, modelled with Ansys HFSS. A simplified cross-section view of the thruster is included at the bottom of the figure for reference, with the same colour code as in figure 1. Solid and dotted lines correspond to relevant magnetic field lines, passing by the boundaries of the ionisation chamber (grey), the sides of the coaxial termination (purple) and the centre of the coaxial termination (pink).

Power is brought to the source thanks to the coaxial TL with 7-16 DIN standard connectors. The 7-16 DIN standard connectors provide greater microwave power at 2.45 GHz. This frequency has been chosen as it has been the reference in many previous studies. The TL is detailed in Figure 3. Microwaves are generated by a solid-state microwave generator MR1000D-200ML from Muegge with a power range of $10-1000$ W and a frequency of 2.45 GHz$\pm$50 Hz. To pass through the vacuum chamber, a 7-16 DIN coaxial feedthrough is used, followed by an assembly of two rectangular waveguide-to-coaxial adapters, acting as a DC-block. A 3 dB coaxial three-way splitter is used to divide the microwave power between the sources. The adaptation of the impedance of each source to the plasma might slightly modify the amount of power forwarded and reflected to the sources by the splitter. Finally, each source is equipped with a 7-16 DIN receptacle panel (3) mounting ended by a M3 central rod. The latter fixes a coaxial termination (4), inserted in the ionisation chamber and in contact with the plasma.

Finally, the plasma source can be decomposed into four distinct parts: the gas injection (5), the prechamber (6), the internal ceramic, the external ceramic (7) and the ionisation chamber (8). The ceramic parts isolate electrically the coaxial termination from the ionisation chamber. At last, it reaches the ionisation chamber. Dimensions are detailed in Table 1. This assembly is kept electrically floating.

Figure 4 shows the cluster in operation in the EPIC-2 vacuum chamber. A high mass flow rate has been set to each source (20 sccm). The naked-eye observation of the plume is not symmetric with regard to the horizontal plane. Indeed, a small fraction of the plasma appears to deviate to the upper side (i.e. in the y direction). This fraction increases along with the mass flow rate. This unwanted feature remained unaltered regardless of attempts to correct it: sources have swapped one with another, N42 magnets have been rotated and flipped, y offset has been applied in between the permanent magnets and the sources, etc... The main hypothesis was aimed towards an asymmetry in the B-field, however the latter has been probed and measurements match with simulation data.

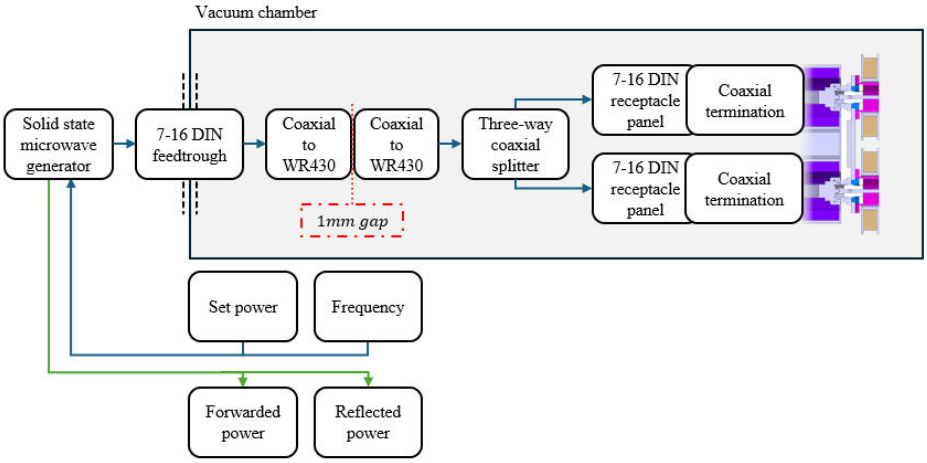

Figure 3. Transmission line of the cluster.

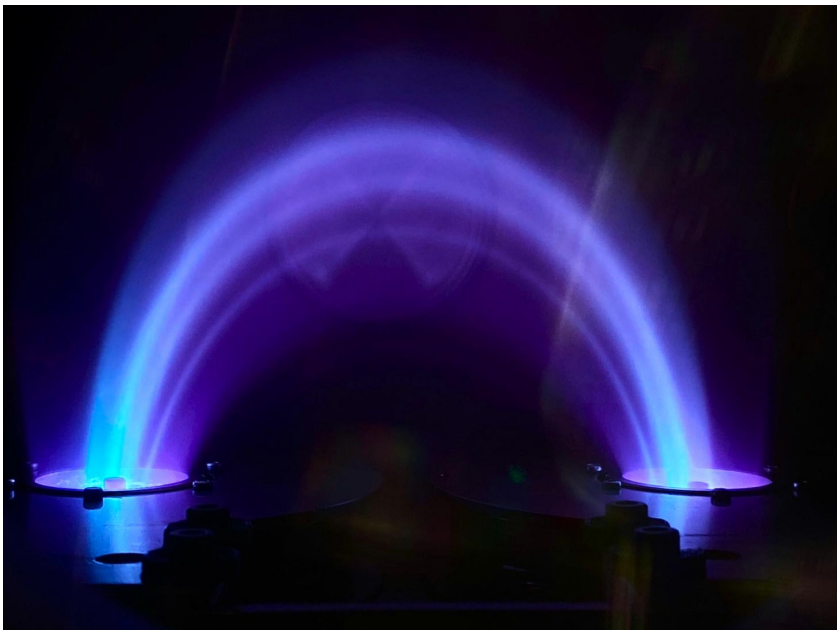

Figure 4. Cluster in operation in EPIC-2 with 20 sccm of Xenon on each source, 4 A applied to each of the magnetic nozzle coils and 100 W of microwave power at 2.45 GHz split before the ionisation chambers. The shift between the plasma beam and the coaxial termination on the highest source is due to a misalignment default.

Ionisation chamber length	20 mm
Ionisation chamber internal diameter	30 mm
Coaxial termination length immersed in plasma	20 mm
Coaxial termination diameter	4.5 mm
ECR magnetic field	875 G
Maximum electromagnet power per source	15 W
Total number of turns for MN per source	≈ 400

Table 1. Cluster of two ECR sources main characteristics.

B. Electrostatic probes setup

The electrostatic probes measurements have been conducted in the Laboratory of Space Propulsion of Universidad Carlos III de Madrid, Leganés, Spain. More details about the facility can be found in previous works [13,14]. The vacuum chamber in use has a length of 3.5 m and an internal diameter of 1.5 m. A total pumping capacity of 37000 l/s for Xenon is reached thanks to three types of pumps: a primary Leyvac LV80 dry pump with a pumping capacity of 80 m^3/h, two Leybold MAGW2.200iP turbomolecular pumps with a pumping capacity of 2000 l/s, three Leyvac 140 T-V cryopanels reaching down to 20 K.

This vacuum chamber can reach pressure down to 10^{-7} mbar in dry conditions. The mass flow rate range used in the electrostatic probe measurements is in the range of 1 sccm to 10 sccm per source. Pressure stays in the range $\left[2.5 \times 10^{-6} - 2.5 \times 10^{-5}\right]$ mbar. A single bottle of Xenon is linked to a Bronkhorst EL-FLOW Select Xenon calibrated mass flow controller (accuracy of 0.1 sccm, maximum mass flow rate of 100 sccm). The gas feeding line is split just before the thruster by a Swagelock T gas-splitter. The distance between the cluster exhaust plane and the end of the vacuum chamber is 2.5 m.

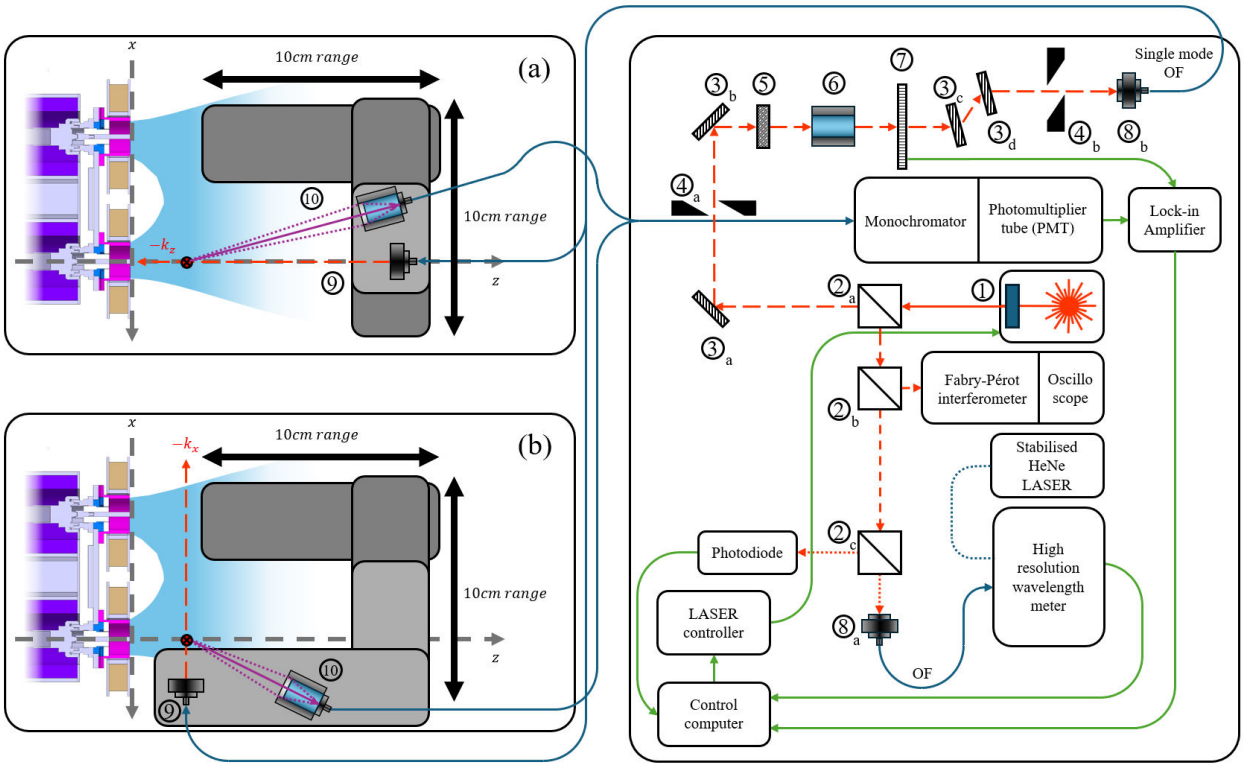

Figure 5. Diagram of the LIF optical bench with in-vacuum optics. (a) Axial velocity configuration and (b) Radial velocity configuration. 1. Tunable single-mode laser diode and powermeter 2. Beam splitters 3. Mirrors 4. Diaphragms 5. Half-wave blade 6. Polariser 7. Mechanical chopper 8. Collimators 9. Laser injection 10. Detection branch.

Three electrostatic probes have been used to assess the plasma properties. The Faraday Cup (FC) has an aperture with a diameter of 10 mm. The current density is obtained by dividing the collected current by the area of collection (i.e. 70 mm^2).

The Langmuir Probe (LP) has an exposed tip of 7 mm, with a diameter of 0.25 mm. IV curves are obtained by sweeping the voltage applied to the LP and measuring the collected current. Raw data is processed following Lobbia et al. [15] recommended practices. The ion density, the electron temperature and the plasma potential are computed from the IV curves. The ion density is computed in regard of the probe radius r_p to Debye length λ_D ratio, and refined through iterations of the ion saturation current $I_{i,sat}$ until convergence. The electron temperature T_e is determined by the slope method. The natural logarithm of the electron current is plotted against the probe bias. A least-squares estimation is made on the linear region in between the floating potential V_f and the V_P. T_e corresponds to the inverse of the least-squares estimation slope. The plasma potential V_P corresponds to the bias of the maximum of the first derivative of the smoothed electron current $dI_{e,smoothed}/dV_B$.

A Retarding Potential Analyser (RPA) [16], used with a control unit both from Impedans Ltd., has been used to determine the ion's most probable energy at points of interest. These latter have been defined thanks to the FC data and consist of plateaux, peaks or drops. The ion's most probable energy can be derived from the IV curves measured by the RPA. However, without measuring the local plasma potential V_p at each measurement, it is impossible to make a correct estimation of the real ion kinetic energy.

One at a time, the FC and RPA have been mounted on an azimuthal translation arm. It has been centred on the plane of symmetry in between the sources, with its origin being defined as the cluster exhaust plane. It allows to move the probes from $-90°$ to $90°$ with a step of $1°$. Moreover, the probes can be moved in the radial direction from 0 mm to 400 mm, with a minimal step of 0.3 mm. Both probes were aligned with the arm axis. Measurements have been performed at 280 mm from the origin for the FC, and 380 mm for the RPA. The LP has been mounted on the same translation azimuthal translation arm, set at $0°$ and swept from 50 mm to 300 mm with a 1 mm step.

C. LIF setup

The LIF measurements have been realised in the ICARE Laboratory of the CNRS of Orléans, France. First ignitions have been made in the EPIC-2 vacuum chamber (54 cm in radius, 104 cm in length, Edwards GV110 main dry pump and 2 STP-iS2207 turbomolecular pumps, 10^{-4} mbar with 20 sccm of Xe). LIF measurements have been performed in the New Experiment on Electric Thrusters (NExET) vacuum chamber. With a length of 1.8 m and an internal diameter of 0.8 m, this chamber is equipped with an Edwards GV110 main dry pump and a STP-iS2207 turbomolecular pump. In addition, a cryopanel localised at the bottom centre of the chamber reaches temperatures down to 50 K. A dry pressure of 10^{-6} mbar can be reached, with an average pressure of 5×10^{-5} mbar with a total input mass flow rate of 5 sccm. A Xenon bottle is connected to two independent Alicat 20 sccm Flow Meter mass flow controllers by a Swagelock T gas-splitter. Each controller is linked to a source.

1. LIF physical principle

The ion velocity can be determined by Laser Induced Fluorescence (LIF) along the laser beam direction by measuring the Doppler shift of absorbed photons. The isotropic fluorescence occurs when a probed ion, excited by the laser, deexcites to a lower energy state and emits a photon. The excitation from one quantum level to another happens when the photon matches the energy difference in between the two levels. As selection rules bound the energies allowed for the previously stated transitions, a specific species can be studied. Measuring the frequency at which the laser beam energy is absorbed allows the determination of ion Doppler shift, hence its velocity depending on the laser beam direction: $\Delta\nu = \nu - \nu_0 = \frac{1}{2\pi}\boldsymbol{k}\cdot\boldsymbol{v}$
$\nu_k = c\frac{\nu-\nu_0}{\nu}$ where $\Delta\nu$ represents the Doppler shift, ν the laser frequency, ν_0 the studied transition unshifted frequency, $\boldsymbol{k}$ the laser beam wave vector, $\boldsymbol{v}$ the velocity vector of the studied particle, v_k its velocity parallel to $\boldsymbol{k}$ and c the speed of light. By sweeping the laser frequency, the Velocity Distribution Function (VDF) can be determined. Indeed, the fluorescence signal intensity is proportional to the density of the particles for a given frequency. Thus, a frequency sweep associates a shift—i.e. a velocity—to a (relative) density. Table 2 details the Xenon ions (Xe II) population probed in the metastable level.

		Transition	λ air (nm)
Xe II	Excitation	$5s^2 5p^4 \left(^3P_2\right) 5d^2 \left[4\right]_{7/2} \rightarrow 5s^2 5p^4 \left(^3P_2\right) 6p^2 \left[3\right]^\circ$	834.72
	Fluorescence	$5s^2 5p^4 \left(^3P_2\right) 6p^2 \left[3\right]^\circ \rightarrow 5s^2 5p^4 \left(^3P_2\right) 6s^2 \left[2\right]_{3/2}$	541.91

Table 2. Probed optical transitions, excitation and fluorescence wavelengths in LIF.

2. Optical bench

Figure 5 depicts the two configurations used for LIF spectroscopy measurements. The same configurations are used with a single source. Configuration (a) focuses on measuring the ion axial velocity, whereas configuration (b) on radial velocity. Regardless of the configuration, this setup allows us to perform time-averaged LIF. First of all, a laser beam is produced by an amplified tunable single-mode external cavity laser diode (1) represented by the red path on the scheme. This diode can deliver up to 700 mW of power in the near-infrared spectral domain. The laser remains mode-hop free over a frequency tuning range of more than 20 GHz. A powermeter is juxtaposed to the diode to guarantee that the power density remains in the order of a few mW.mm^{-2} to avoid the saturation of the natural line shape. A first Beam Splitter (BS) $(2)_a$ divides the beam into two main paths. The first one aims to analyse the emitted laser beam, whilst the second brings the beam to the thruster. Focusing on the laser beam analysis, a second BS $(2)_b$ directs part of the beam to a Fabry-Pérot interferometer (with a 1 GHz free spectral range), linked to an oscilloscope. The latter is used to check both the quality and the stability of the laser mode in real time. Mode hops can occur through the laser wavelength sweep (as the electric intensity of the diode decreases). These hops are to be avoided to obtain a smooth sweep. Moreover, they can in addition be checked on the oscilloscope. The remaining part of the laser beam encounters a third BS $(2)_c$, which splits the beam towards a photodiode and a collimator $(8)_a$. The photodiode goal is to measure the laser beam intensity at all times and to communicate it to the control computer. The collimator $(8)_a$ is linked to a high-resolution wavelength meter by an Optical Fiber (OF). The wavemeter measures the real-time laser beam wavelength and outputs the latter to the control computer. It is calibrated using a HeNe stabilised laser with a 632.9914 nm wavelength. The second main laser beam emitted towards the thruster begins by being reflected on a first mirror $(3)_a$, before passing through a first diaphragm $(4)_a$ and being reflected on a second mirror $(3)_b$. The half-wave blade (5) and the polariser (6) guarantee that the beam is linearly polarised. The mechanical chopper (7), linked to the lock-in amplifier, has a modulation frequency of 1443Hz. After being reflected on mirrors $(3)_c$ and $(3)_d$, the beam passes through a second diaphragm $(4)_b$ to focus and is collected by a collimator $(8)_b$. It is then carried by a single mode OF, before being injected in the vacuum chamber (9) with an adapted feedthrough. When measuring the axial velocity, the injection is done in the -z-axis direction. Regarding the radial velocity measurements, the injection is performed on the x-axis direction.

A detection made out of a lens (10) of a 60 mm focal distance focuses the fluorescence light in an OF with a diameter of 200 μm. With a magnification ratio of 1, the spatial resolution of the detection remains the same as the diameter of the OF, i.e. 200μ m. In configuration (a) (axial velocity), the detection branch has an angle of 25° with respect to the injection axis. For configuration (b) (radial velocity), this angle is set to $-25°$ regarding the z-axis. Both the laser injection (9) and the detection branch (10) are mounted on two Newport linear translation stages with a 10 cm range. A 10 cm$\times$10 cm surface can be covered, with a minimum step of 10^{-3} mm. The x-axis is aligned with the sources exhaust plane, its origin being localised at the coaxial termination of the source of interest. The z-axis is aligned with the coaxial termination of the source of interest, its origin being localised at the exhaust plane of the source. The OF originating from the detection branch (10) passes through an adapted feedthrough and is linked to a monochromator. The latter isolates the fluorescence wavelength of interest from the rest of the spectrum. Finally, a photomultiplier acts as a light detector, converting the light into an electrical signal. The chopper and the photomultiplier are both connected to a lock-in amplifier, matching their frequencies to discriminate the fluorescence light from the plasma emission. The control computer receives as inputs the wavelength of the original beam, its intensity as well as data of the lock-in amplifier. It is connected with the laser controller to sweep the diode frequency. A software controls all the previously stated components.

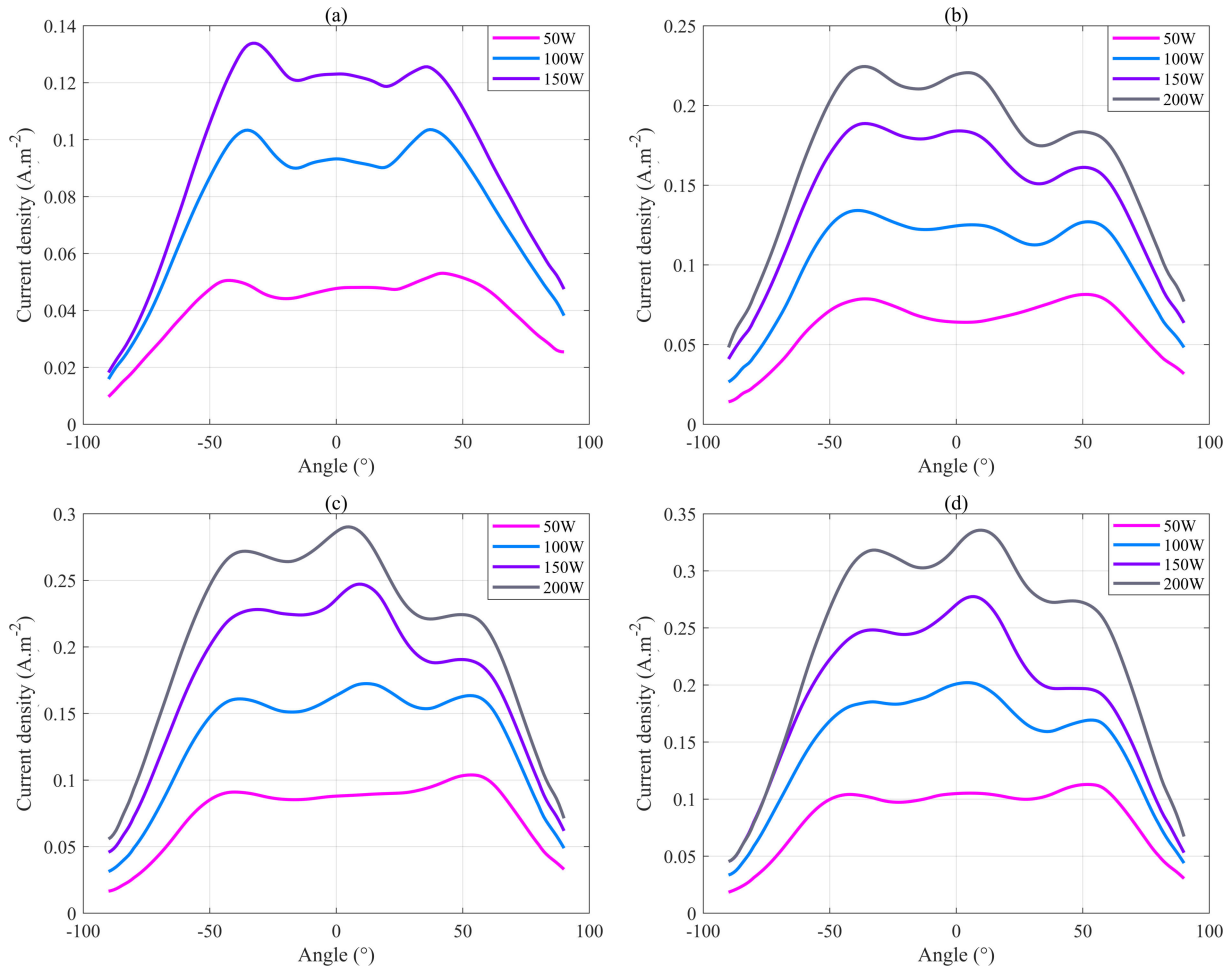

Figure 6. Current density measurements on the two-ECRT cluster in a power range from 50 W to 200 W. 2 A is set on each MN coil. (a) 5 sccm, (b) 10 sccm, (c) 15 sccm, (d) 20 sccm.

III. Plume characterisation using electrostatic probes

In the following, power varies from 50 W to 200 W, whilst the mass flow rate ranges from 5 sccm to 20 sccm. Measurements have been taken at a radius of 280 mm from the thruster exit for the FC and 380 mm for the RPA.

1. FC measurements

Figure 6 depicts the current density measured by the FC at multiple microwave power for different mass flow rates. First, the current density increases along with the mass flow rate and the microwave power. It is to be noted that the peaks on both sides of the symmetry plane are of higher amplitude than the one localised at 0° for a mass flow rate of 5 sccm in Figure 6(a). Figure 6(b) shows the current density for a mass flow rate of 10 sccm. A peak with an amplitude close to the side peaks is present at 0°. Increasing the mass flow rate could increase the current density of the plasma resulting in the merging of the beams. This effect is more noticeable in Figures 6(c) and 6(d), with respectively 15 sccm and 20 sccm of Xenon. Some asymmetries in terms of current density can be noticed, regardless of the operation point. Their origins could be varied: e.g. misalignment of the elements in the ionisation chamber, disequilibrium in the mass flow rate distribution between the sources, mismatched TL impedance after the splitter and difference in plasma impedance in each source.

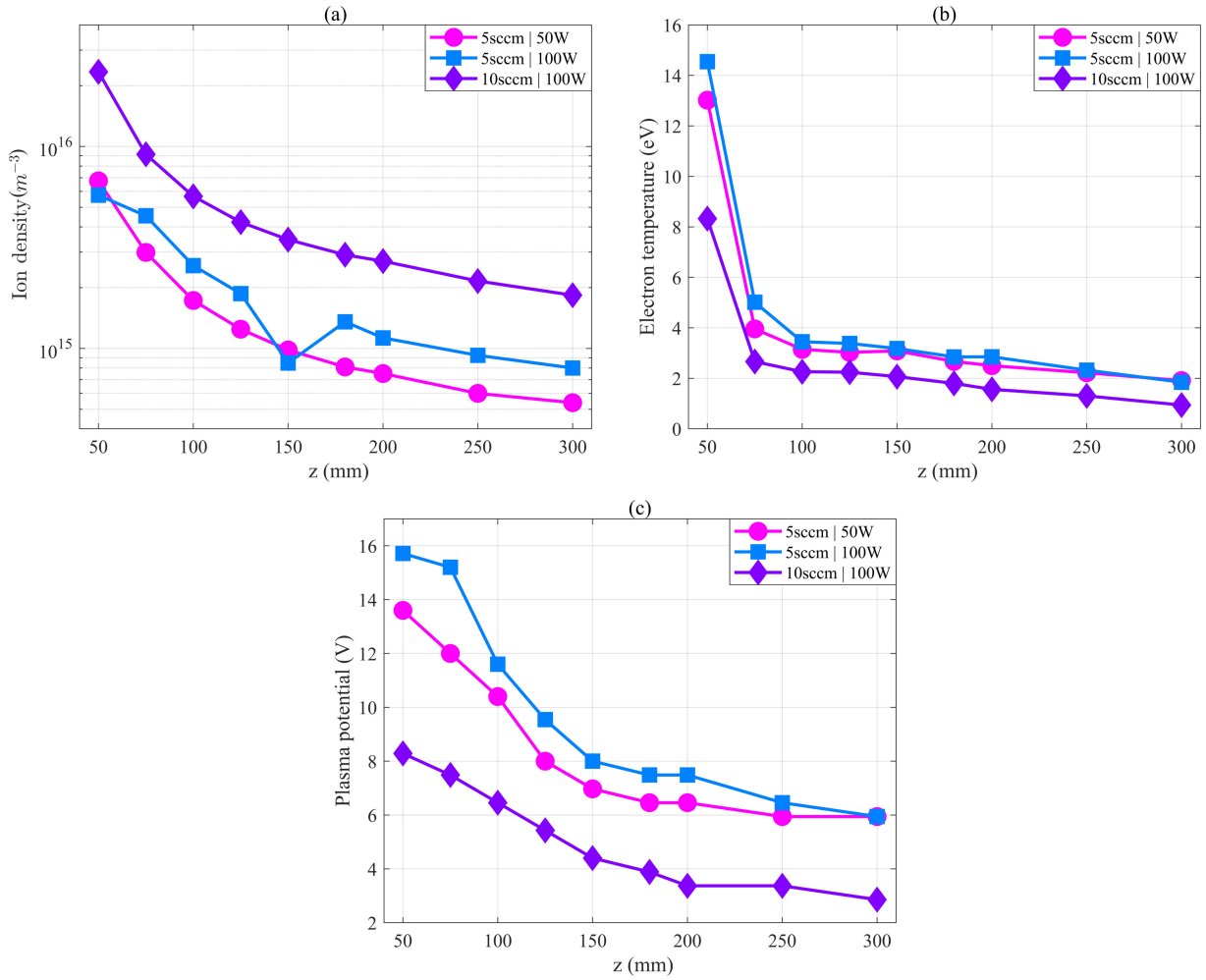

Figure 7. LP measurements on the MAT3 cluster for different operation points: 5 sccm with 50 W, 5 sccm with 100 W and 10 sccm with 100 W. 2 A is set on each MN coil. (a) Ion density n_i, (b) electron temperature T_e, (c) plasma potential V_p.

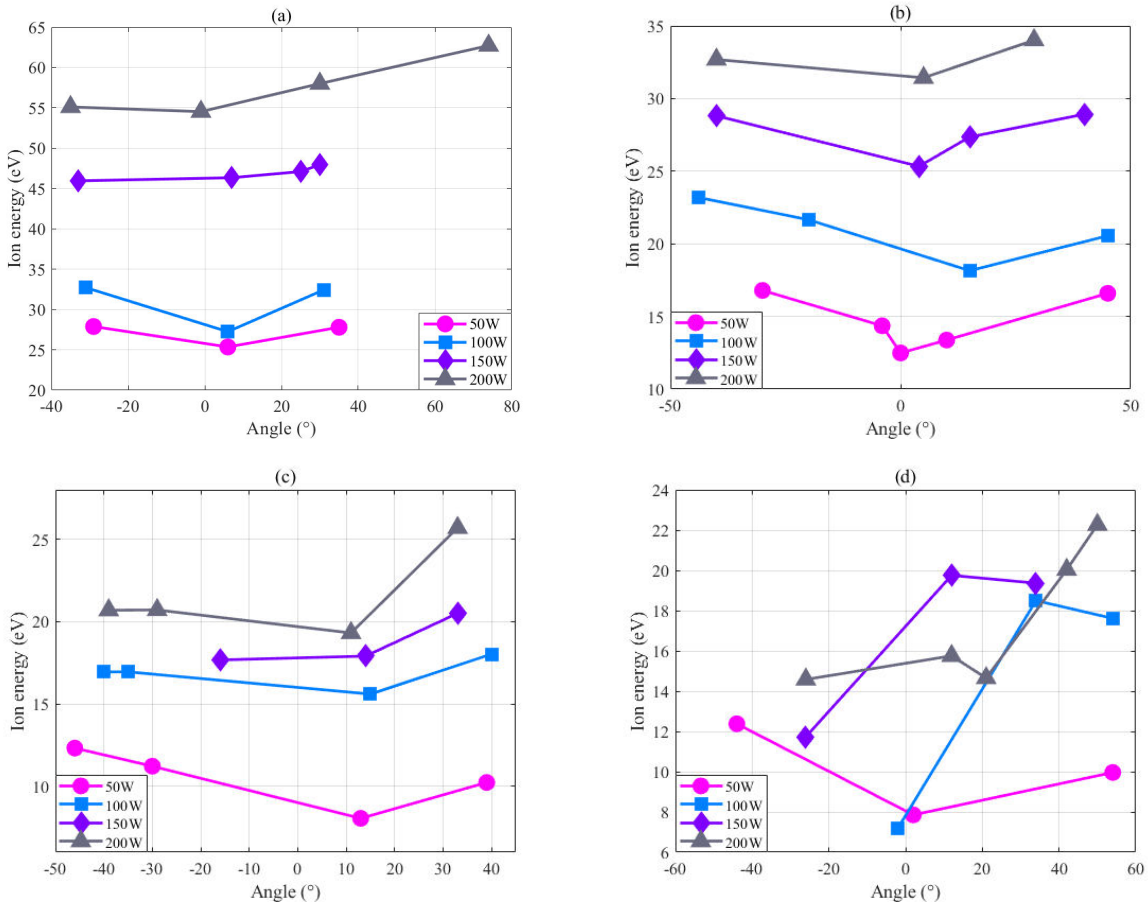

Figure 8. RPA measurements on the cluster in a power range from 50 W to 200 W. 2 A is set on each MN coil. (a) 5 sccm, (b) 10 sccm, (c) 15 sccm, (d) 20 sccm.

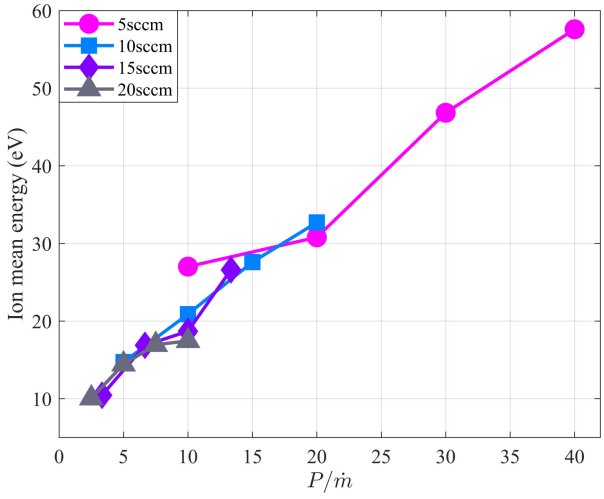

Figure 9. Mean of ion most probable energy as a function of the power to mass flow rate ratio, measured at different mass flow rates: (a) 5 sccm, (b) 10 sccm, (c) 15 sccm, (d) 20 sccm. 2 A is set on each MN coil.

2. LP measurements

Only three operation points have been studied: 5 sccm with 50 W, 5 sccm with 100 W and 10 sccm with 100 W. Measurements have been taken along the axis corresponding to the intersection between the horizontal plane and the plane of symmetry of the cluster. The ion density, shown in Figure 7(a), decreases along the z-axis. However, it drops by one order of magnitude in between 50 mm and 300 mm. The ion density increases along with the microwave power and the mass flow rate. The ion density remains low when compared to similar thrusters [7,17]. However, it is to be reminded that the measurements have been made on a vertical axis 60 mm away from both sources' centerlines.

Figure 7(b) depicts the electron temperature. From these results, the mass flow rate arguably has a stronger influence on the electron temperature than the power. A sudden drop to about 1/3 of the temperature occurs, regardless of the operation point, from 50 mm to 100 mm. Indeed, for the 5 sccm with 100 W operation point, a maximum electron temperature of nearly 15 eV drops to three times less at 5 eV. Following the magnetic field lines shown in Figure 2, it appears that the magnetic field line closing the external part of both sources is localised at nearly 90 mm. As electrons tend to follow magnetic field lines, it could be hypothesised that electrons with higher energy remain enclosed in the magnetic arch. However, electron cooling could also take place in the cluster symmetry plane, along with losses of energy due to ionisation, collision, etc. Nevertheless, electrons present temperatures similar to ones found in other ECRTs.[7,17]

Plasma potentials, presented in Figure 7(c), are relatively low compared to previous ECRT works [7,17,18], with a maximum of 16 V being measured for the 5 sccm with 100 W operation point. The latter presents the highest plasma potential of the three.

3. RPA measurements

RPA measurements are presented in Figure 8. As detailed in Section II.B, these measurements have been performed at points of interest defined thanks to FC data (such as plateaus, peaks or drops). Mass flow rates vary from 5 sccm to 20 sccm, with a power range between 50 W to 200 W. First of all, the ion's most probable energy decreases with increasing mass flow rate, as the same microwave power is presumably divided over a larger amount of propellant. Figure 8(a) focuses on a mass flow rate of 5 sccm. Most probable ion energy profiles are quite constant for each power, from an average of 27 eV for 50 W to 60 eV for 200 W. The same average energy can be found for half the power (100 W) whilst the mass flow rate has doubled (10 sccm) in Figure 8(b). For this mass flow rate, average energies have been divided by 2. This trend continues from 10 sccm to 15 sccm, as seen in Figure 8(c). However, the average most probable energies seem to be similar for both 15sccm and 20 sccm as it can be seen in Figure 8(d). Figure 9 shows the evolution of the ion mean energy as a function of the power-to-mass flow rate ratio. The increase is linear (with a slope of 4/3) and measurements performed with different mass flow rates overlap.

IV. Ion velocity vector determination using LIF

A. Single source

Figure 10 presents the position of the probed points used for both the axial and the radial components of the velocity. The x-axis and z-axis are respectively centred on the single source exhaust plane and the coaxial termination. Measurements are limited in space and resolution because of the low plasma density farther downstream—as the signal intensity is proportional to the Xe II density. Only the right part of the source concerning the z-axis has been probed. Four radial measurements have been performed on the left part to test the source axisymmetry.

Figure 11 depicts a single source's axial ion velocity mapping. It increases along the distance from the cluster exhaust plane, with a maximum obtained at $[x = 0\,mm, z = 60\,mm]$ with 6.5 km/s. It tends to decrease when getting farther from the z-axis. Measurements have been performed also inside the ionisation chamber (i.e. $z < 0$ mm), where ions present a low axial velocity ($1 < v_z < 2$ km/s) as the acceleration is realised downstream.

The radial component of the velocity vector can be seen in Figure 12. Measurements have been performed on both sides of the z-axis to check the symmetry in terms of radial velocity. Table 3 regroups the radial velocity magnitude for points localised on both sides of the z-axis. On the latter, the magnitude does not exceed $|-0.2|$ km/s. It acts as a separatrix between the positive and negative velocities. Velocities tend to

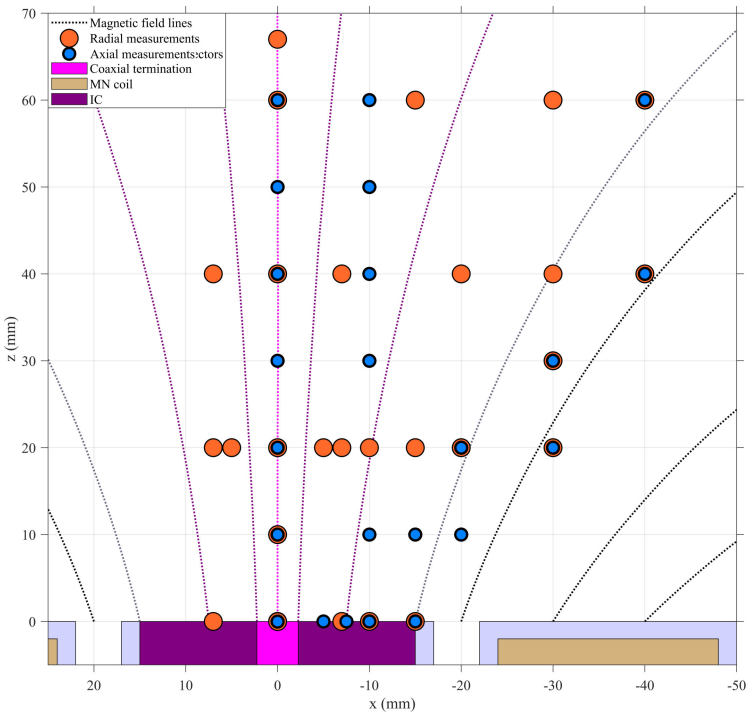

Figure 10. Xe II measurements position for a single source, overlapped with a cross-section top view of a single source. The magnetic nozzle coil is displayed in brown, the boundaries of the IC in grey, the spaces between the latter and the coaxial termination in purple and the coaxial termination in pink. Magnetic field lines of interest are displayed with dotted lines $[x = [-15, -10, -7.5, -2.25, 0, 2.25, 7.5, 10, 15]\ mm, z = 0\,mm]$. Orange circles represent radial measurements, and blue circles axial measurements.

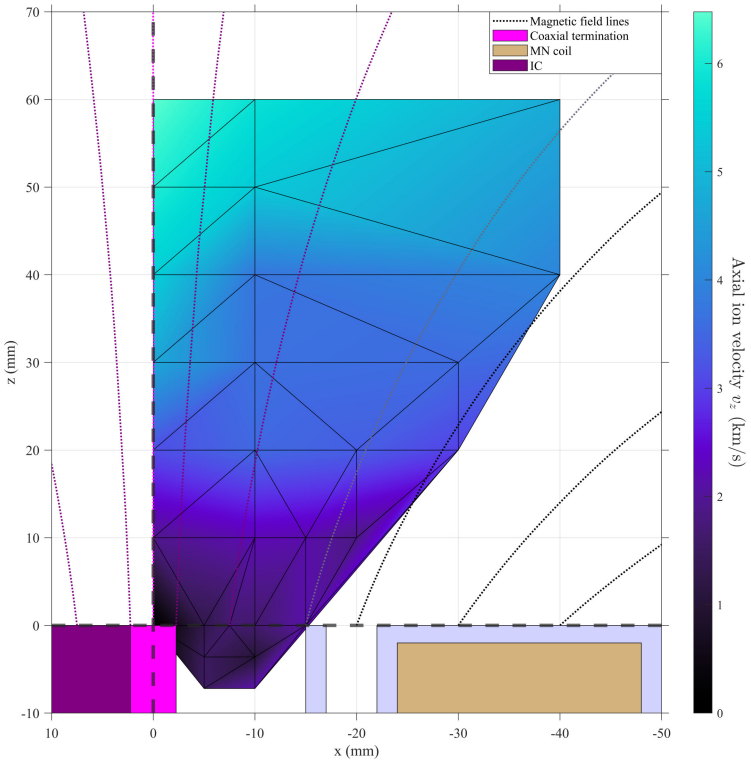

Figure 11. Xe II axial velocity colormap for a single source. The left part of the IC has not been shown to plot the axial velocity in the IC. Operation point: 2.5 sccm, 50 W, 2 A on the MN.

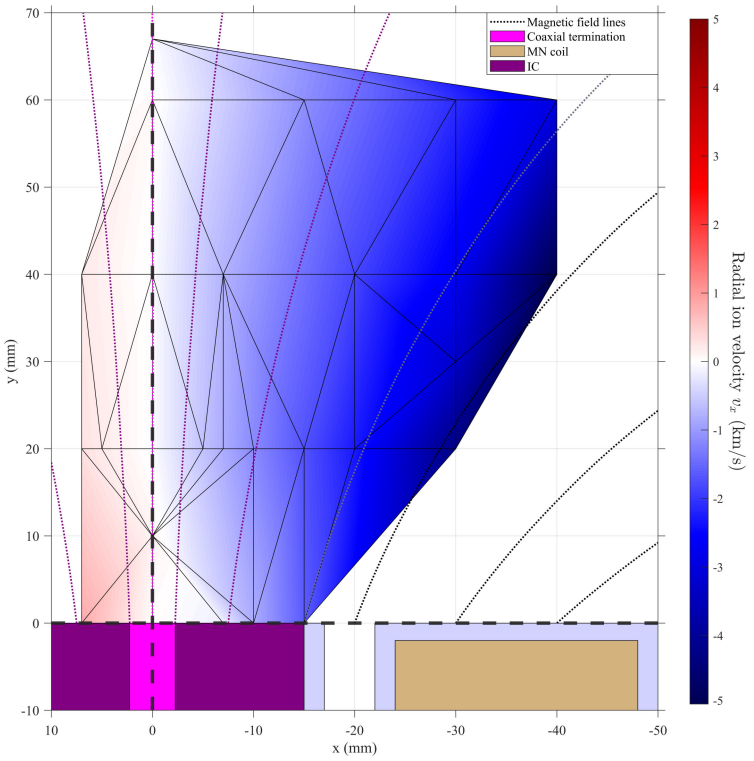

Figure 12. Xe II radial velocity colormap for a single source. Operation point: 2.5 sccm, 50 W, 2 A on the MN.

be higher in magnitude by some hundreds of m/s on the right part of the z-axis. This slight difference can be explained by misalignment in the source assembly or between the laser injection and the source. Still, the source can be considered as axisymmetric. The radial velocity increases along with the distance to the z-axis, with a maximum being found at $[x = -40\,mm, z = 40\,mm]$ with $|-5.1|$ km/s. Moreover, it decreases along with the z-axis.

z (mm) / x (mm)	0	20	40
-7	-0.15	-0.8	-0.75
-5	N/A	-0.6	N/A
0	N/A	-0.02	-0.02
5	N/A	0.2	N/A
7	0.8	0.3	0.2

Table 3. Radial velocities on both sides of the z-axis (km/s).

Figure 13 depicts the colormap of the in-plane velocity magnitude on its left, as well as the velocity vectors and ion streamlines on its right. The velocity magnitude is made out of its axial and radial components, as the azimuthal one is not taken into account. The velocity magnitude increases along with the z-axis and along the distance to the latter. A maximum velocity magnitude of 6.45 km/s can be found at $[x = 40\,mm, z = 30\,mm]$ and $[x = 0\,mm, z = 60\,mm]$.

Ion streamlines detach from the magnetic field lines at the exhaust of the source. However, they essentially become straight downstream ($z > 45$ mm). Collard et al.[19] link the straightening of the ion streamlines to the magnetic field lines by the high decreasing rate of neutral density concerning the decrease in magnetic strength. However, a mass flow rate of 30 sccm has been used in their study, inducing a high neutral density at the source exit. As a mass flow rate 12 times inferior has been used in this study, the ion straightening might occur closer downstream.

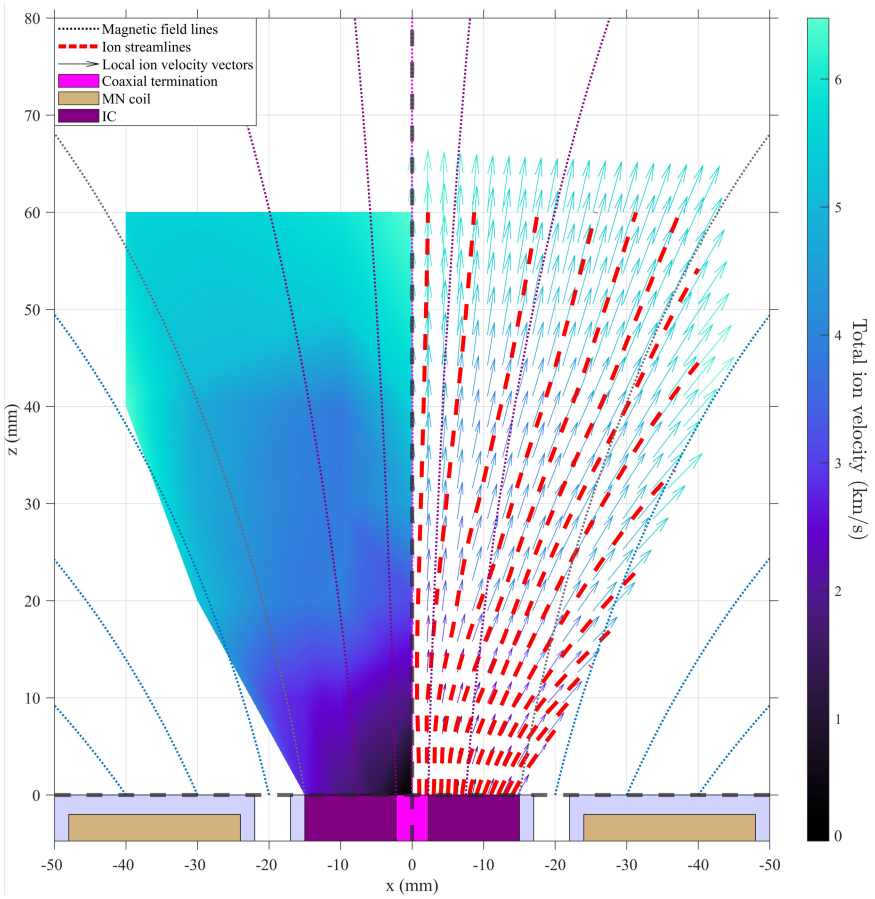

Figure 13. Xe II total local velocity vectors for a single source. The left part represents the velocity magnitude colormap, right part exposes the total local velocity vectors. Ion streamlines, generated at $z = 0$ mm, are displayed in red dotted lines. Operation point: 2.5 sccm, 50 W, 2 A on the MN.

B. Cluster of ECRTs

Figure 14 presents the position of the probed points used for both the v_z and the v_x. The x-axis and z-axis are respectively centred on the left source exhaust plane and its coaxial termination. Only the left part of the cluster concerning the cluster symmetry plane has been probed. Five v_z measurements have been performed on the right part of the cluster symmetry plane to test the cluster's symmetry.

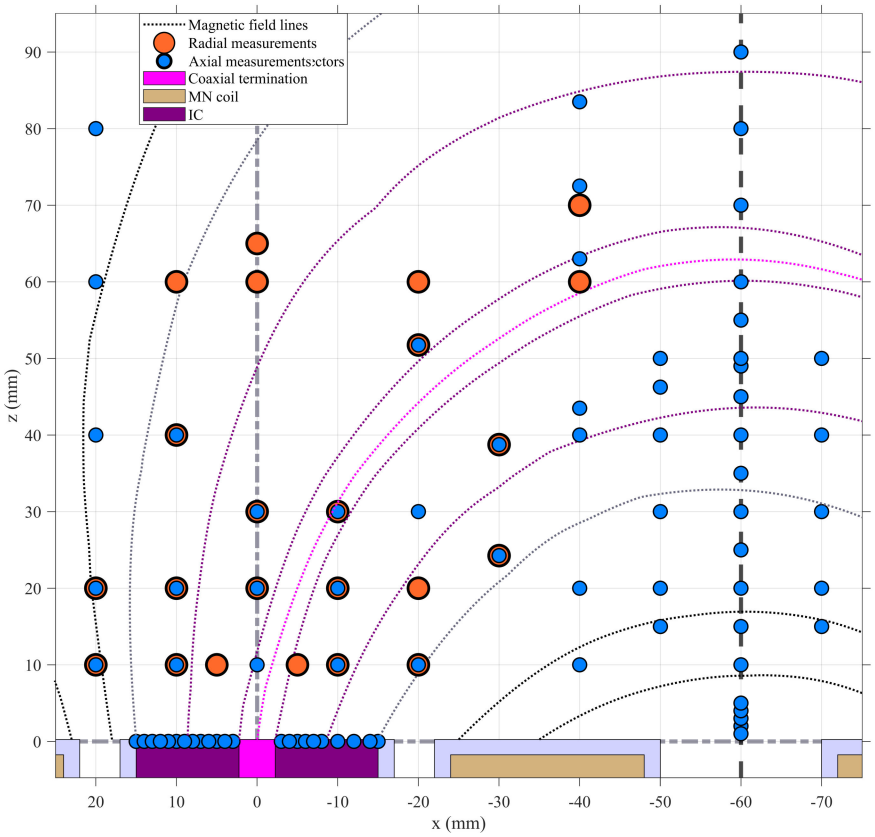

Figure 14. Xe II measurements position, overlapped with a cross-section top view of the cluster. The opposite source is placed 120 mm to the right from the z-axis. The magnetic nozzle coils are displayed in brown, the boundaries of the IC in grey, the spaces between the latter and the coaxial termination in purple and the coaxial terminations in pink. Magnetic field lines of interest are displayed with dotted lines $[x = [-15, -10, -7.5, -2.25, 0, 2.25, 7.5, 10, 15]\ mm, z = 0\,mm]$. The axis corresponding to the intersection between the horizontal plane and the plane of symmetry of the cluster is set at -60 mm. Orange circles represent v_x measurements, and blue circles v_z measurements.

Figure 15 represents the evolution of the VDF along the left source exhaust plane, on both sides of the coaxial termination (i.e. $[x = [-15 : 15]\ mm, z = 0\,mm]$). First of all, an asymmetry in terms of VDF can be observed on both sides. This asymmetry is likely a consequence of the asymmetric magnetic topology within the source. The VDFs for $x < 0$ mm remain distributed around 1.5 km/s, with wider ones at -4 mm and -6 mm. On the left part, velocities increase from 2 km/s at 3 mm to 4 km/s at 9 mm. From 10 mm on, a second peak is observed around -2.5 km/s. This peak has not been observed closer to the coaxial termination. Its arising could be linked to the crossing of the source exhaust plane and the magnetic field lines originating from the metallic ionisation chamber's external metallic walls. Zeeman splitting effect has been considered as an explanation for this second peak, as the magnetic field strength lies around 600 G. Its analysis remains to be done to test this hypothesis.

Figure 16 corresponds to the Xe II v_z along the cluster symmetry plane. v_z increases linearly from 0 mm to 30 mm from the cluster exhaust plane, with a magnitude going respectively from 0 km/s to 1.5 km/s. From 30 mm to 50 mm, a decrease can be observed with a wider VDF at 40 mm. Magnitude goes down from 1.5 km/s back to 0.5 km/s, before increasing again gradually until 90 mm - the maximum distance at which the v_z has been measured. This transition could be linked to the magnetic field lines, as the ones originating from the inside of the ionisation chamber meet the symmetry plane close to 30 mm.

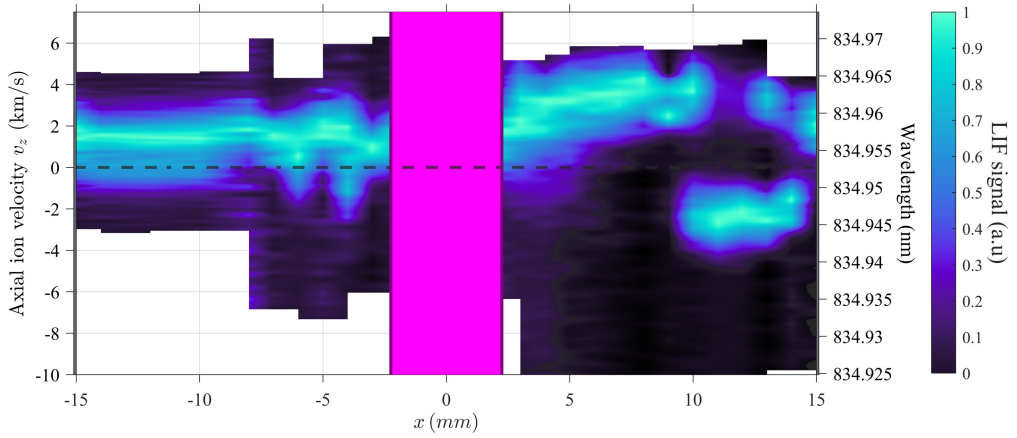

Figure 15. LIF spectrum of Xe II resolved along the right source exhaust plane on both side of the coaxial termination for v_z ($z = 0$mm). The coaxial termination is represented by the pink rectangle. Operation point: 2.5 sccm on each source, 100 W forwarded to the cluster, 2 A on each MN.

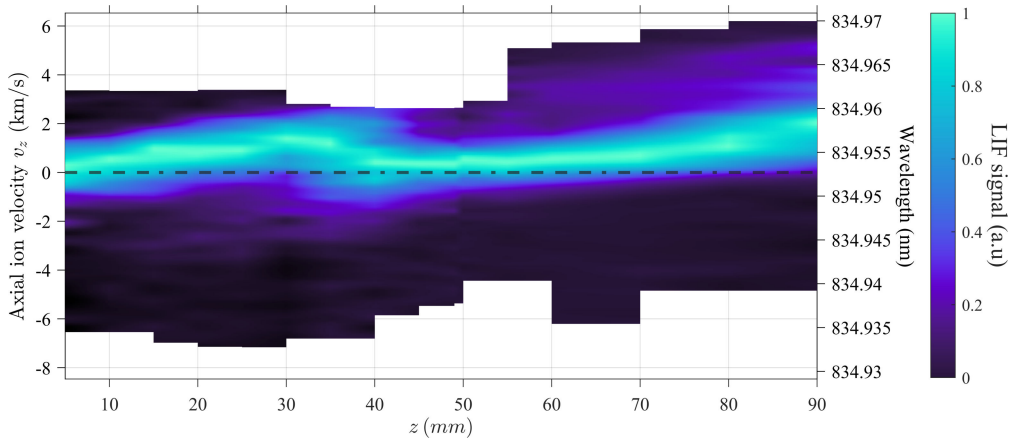

Figure 16. LIF spectrum of Xe II resolved along the cluster symmetry plane for v_z ($x = -60$mm). Operation point: 2.5 sccm on each source, 100 W forwarded to the cluster, 2 A on each MN.

The velocity dispersion σ can be computed thanks to the second-order moment of the VDF [20]. It can be computed thanks to the Full Width at Half Maximum (FWHM) p of the Gaussian approximation of the VFDs. The link between the FWHM and the velocity dispersion is:

$$\sigma = \frac{p}{2\sqrt{2\,ln\,(2)}}. \tag{1}$$

An ion temperature approximation T_i can be obtained from the velocity dispersion using the Boltzmann's constant k_B and the ion mass m_i:

$$T_i = \frac{m_i \sigma^2}{k_B}. \tag{2}$$

Figure 17 depicts the evolution of the ion temperature along the cluster symmetry plane, based on spectra shown in Figure 16. An peak can be seen between 30 mm and 50 mm. As aforementioned, this range corresponds to the localisation of the magnetic field lines originating from the inner part of the IC (i.e. the part closer to the symmetry plane).

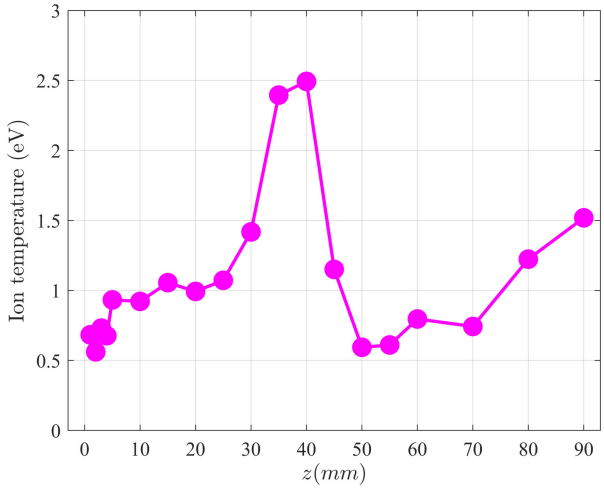

Figure 17. Approximation of the ion temperature based on the velocity spread as a function of the distance from the cluster exhaust plane along the cluster symmetry plane.

v_z has been measured on both sides of the cluster symmetry plane to confirm symmetry between the sources. Five spectra are shown in Figure 18, respectively at 15 mm, 20 mm, 30 mm, 40 mm and 50 mm. Figure 18(c) presents a slight asymmetry from -50 mm to -70 mm, with a wider VDF at -70 mm.

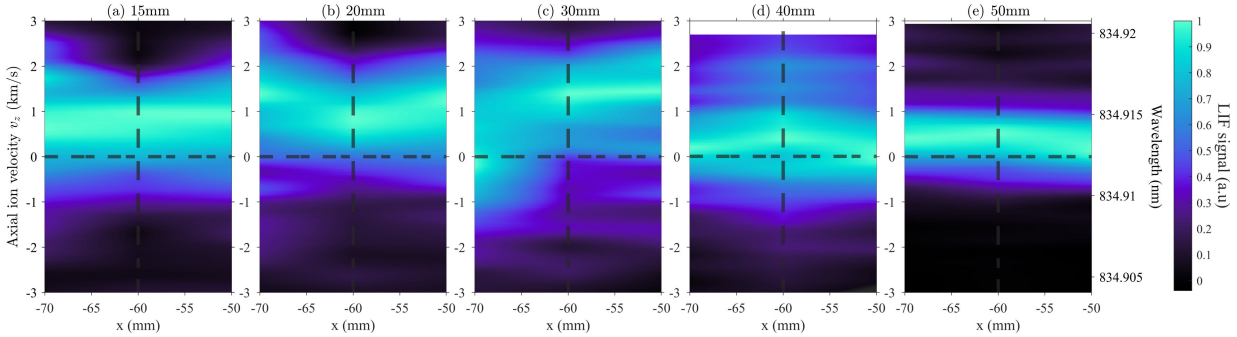

Figure 18. LIF spectra of Xe II resolved on both sides of the cluster symmetry plane for v_z at different distances from the cluster exit plane. Measurements have been taken at $x = -50$ mm, $x = -60$ and $x = -70$ mm. (a) 15 mm, (b) 20 mm, (c) 30 mm, (d) 40 mm and (e) 50 mm. Operation point: 2.5 sccm on each source, 100 W forwarded to the cluster, 2 A on each MN.

Figure 19 focuses on the cluster z component of the velocity. The maximum velocity is measured with 6.65 km/s at $[x = 20\,mm, z = 80\,mm]$. An ion stream generated on the left part of the IC (i.e.

$[x = 3 : 15\,mm, z = 0\,mm]$) is accelerated in a region highlighted by ellipse (1), delimited by the magnetic field line generated at $[x = 7.5\,mm, z = 0\,mm]$. The expansion in this outer region is very similar to that in a single MN.

Under the magnetic field line originating on the coaxial termination side ($[x = -2.25\,mm, z = 0\,mm]$), acceleration is more limited with velocities around 2–3 km/s (i.e. at $[x = -20\,mm, z = 30\,mm]$ and $[x = -30\,mm, z = 24\,mm]$); in this region, and downstream of $z = 40$ mm most of the velocities are close to being null (region represented by ellipse (2)). A last near-zero velocity region is found in the innermost part of the magnetic arch, which is magnetically disconnected from the sources, between $z = 0$ mm and $z = 20$ mm (ellipse (3)).

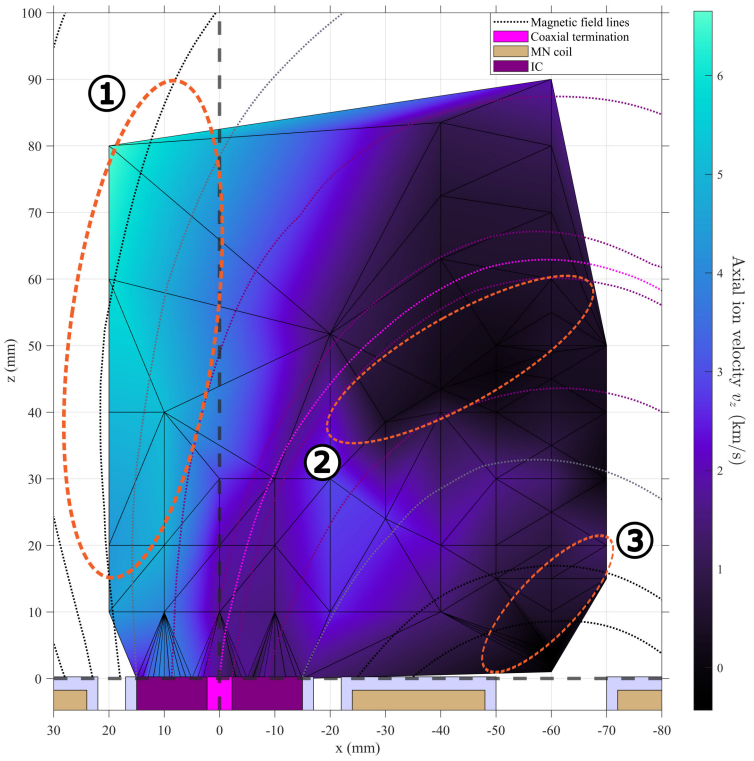

Figure 19. Cluster Xe II v_z colormap. Operation point: 2.5 sccm on each source, 100 W forwarded to the cluster, 2 A on each MN.

The x component of the ion velocity can be found in Figure 20. To begin with, a clear 0 km/s velocity line can be found the parallel z-axis. By extrapolating, it would seem that this line takes its origin 5 mm on the left of the centre of the coaxial termination. The 0 km/s velocity line does not follow magnetic field lines. The v_x is positive/negative on the left/right part of the 0 km/s velocity line, with a maximum of 4.6 km/s measured at $[x = 20\,mm, z = 10\,mm]$. v_x seems to increase along with the distance from the z-axis, with a maximum localised closer to the cluster exhaust plane. The right part of the 0 km/s velocity line presents ions with a negative v_x. As for ions with a positive velocity, negative-velocity ions tend to accelerate along with the distance from the z-axis, with a maximum of $|-4.45|$ km/s at $[x = -30\,mm, z = 24.5\,mm]$. v_x of ions generated under the magnetic field lines originating at the coaxial termination is higher in magnitude.

The in-plane velocity magnitude is computed with v_z and v_x. The azimuthal velocity one is not taken into account, as for the single source configuration. Figure 21 shows the velocity magnitude colormap, as well as the velocity vectors associated. The plasma expansion in the horizontal plane can be divided into two main areas by the z-axis. The outer left part expands as a classical magnetic nozzle compared to Figure 13. However, the velocity vectors plotted in the vertical line originating at $x = 1$ mm have a negative v_x. The maximum velocity magnitude is found at $[x = 20\,mm, z = 10\,mm]$ with 6.4 km/s. Measurements farther away from the cluster exhaust plane at $x = 20$ mm might show an increase in velocity magnitude, as the z component increases and the x one decreases along the z-axis.

The inner, right part shows that ions are more strongly deflected, and there are regions of low velocity where the MA partially confines them. v_x predominates when $x > -20$ mm, and increases closer to the

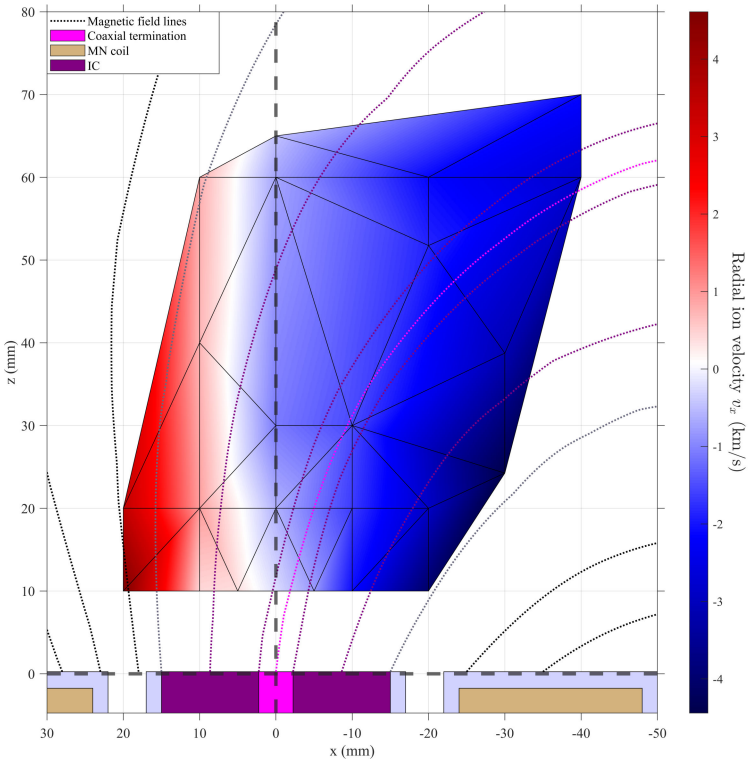

Figure 20. Cluster Xe II v_x colormap. Operation point: 2.5 sccm on each source, 100 W forwarded to the cluster, 2 A on each MN.

cluster exhaust plane. Measurements farther in the plume are necessary to understand the ions' behaviour when crossing the magnetic field lines generated at $[x = 15\,mm, z = 0\,mm]$. Nevertheless, the hypothesis that ions generated for $7.5 > x > 2.25$ mm might have enough v_z to cross the magnetic field lines and escape can be done. Ions generated for $x < 2.25$ mm are slowed by the inner part of the MA and might keep a high v_x, contributing less to thrust. Ions with positive v_x coming from the opposite source should have been probed. The lack of signal for this ion population could be due to the limited lifetime of their metastable state.

V. Summary

Electrostatic probe measurements were performed on the magnetic arch of a cluster of ECR sources with opposing polarities. An increase of the current density along with the power and the mass flow rate (0.05 A.m^{-2} at 5 sccm with 50 W to 0.34 A.m^{-2} at 20 sccm with 200 W) can be noted. A central peak arises on the cluster symmetry plane in terms of current density along with the increase of power and mass flow rate. For low power and mass flow rate, only peaks localised around $|[40°; 50°]|$ are present. They face the exhaust of each source. LP measurements have been realised at the intersection between the horizontal plane and the plane of symmetry of the cluster. Ion density have been measured up to $\left[10^{15}; 10^{16}\right]$m^{-3} in the cluster symmetry plane. A drop of the electron temperature takes place along the z-axis in the cluster symmetry plane. As electrons are magnetised and following magnetic field lines, this could be linked to different populations inside and outside the magnetic arch. Still, electron cooling happens in classic ECRTs [7] without closed-line magnetic topology. The plasma potential decreases along with the distance to the cluster exhaust plane. The most probable ion energy, from RPA measurements, increases along with the increase of power, but decreases along with the increase of mass flow rate. Ion's most probable energy mean value increases linearly along with the power to mass flow rate ratio with a slope of 4/3.

A 2D velocity vector map has been measured for a single ECR source using LIF. v_z increases along with the distance to the source exhaust plane. Axial velocities up to 6.5 km/s have been probed, with a maximum

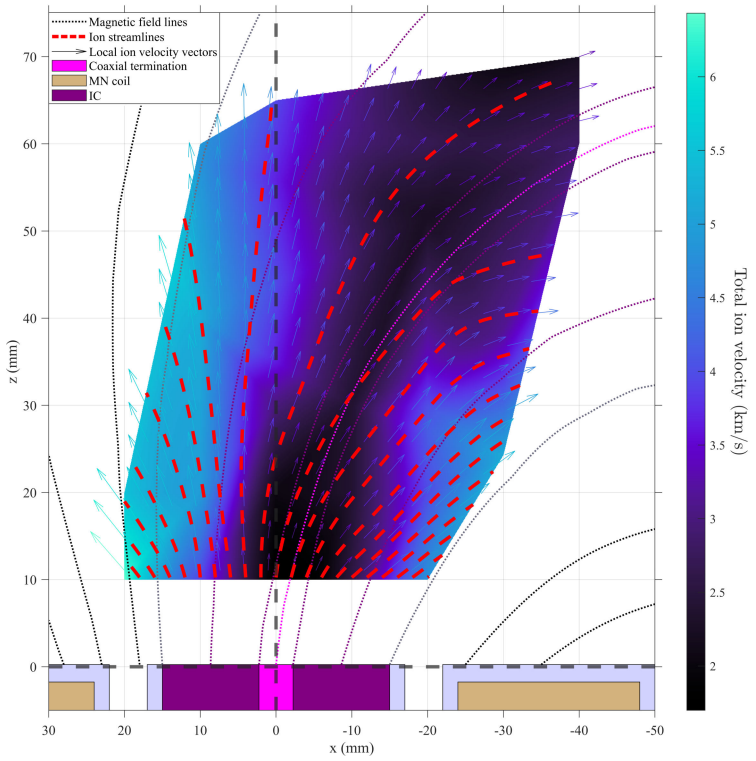

Figure 21. Cluster Xe II velocity magnitude. Velocity local vectors overlap the colormap of the velocity magnitude. Ion streamlines are displayed in red dotted lines. Operation point: 2.5 sccm on each source, 100 W forwarded to the cluster, 2 A on each MN.

distance of 60 mm to the exhaust plane. v_x increases along with the distance to the source centerline. v_x up to $|-5.1|$ km/s have been measured. Axisymmetry has been observed in the source thanks to measurements on both sides of the centerline. Ion streamlines detach from the magnetic field lines at the exhaust of the source, locally diverging faster than magnetic lines in some regions, before becoming essentially straight downstream ($z > 45$ mm).

The velocity magnitude map of a cluster of two ECR sources spaced by 120 mm centerline to centerline has been realised. The neighbourhood of the left source has been mapped. Symmetry in the cluster is supported by measurements of v_z on both sides of the cluster symmetry plane. A possible Zeeman splitting effect can be witnessed near the left source exhaust plane. Modelling of the fluorescence lineshape is necessary to assess its presence regarding a possible existence of a lower velocity ion population. A variation in v_z has been probed in the cluster symmetry plane. v_z increases from $z = 0$ mm to $z = 30$ mm, before decreasing from $z = 30$ mm to $z = 50$ mm. It only increases past $z = 50$ mm. This variation localisation matches with the magnetic field lines emitted at the coaxial terminations of the sources. This variation can also be seen with the approximation of the ion temperature by the velocity dispersion. v_z mapping of the cluster shows high velocities on the external side of the latter (i.e. $[x < -120\,mm]\mathrm{U}[x > 0\,mm]$). However, v_z decreases inside the magnetic field lines closing the magnetic field arch (generated at $[x = 20\,mm, z = 0\,mm]$) with near-zero axial velocities localised near the magnetic field lines generated at the sources coaxial termination ($[x = 0\,mm, z = 0\,mm]$). A zero v_x line goes along the z-axis, parallel to the centerline of the left source. It separates the v_x map in two, with positive velocities on its left (external side) and negative ones on its right ($[-140\,mm < x < 20\,mm]$). For $x > 0$ mm, the ion streamlines follow the same behaviour as for the single source. However, ion streamlines show that ions are trapped in the closed-line magnetic topology as they present a near-zero v_z near the cluster symmetry plane. As the lifetime of the Xe II metastable state is limited, it remains impossible to conclude the trajectory of the ions trapped in the magnetic field arch. They could present a fully-radial trajectory, or be impacted enough by the ambipolar field to be directed to the opposite source exhaust.

The study allows concluding that the MA is a viable magnetic configuration for the electrodeless and contactless generation of a free plasma jet, albeit the ion energy is likely lower than in a comparable MN due to the partial confinement exerted by the inner magnetic lines on the plasma, in agreement with previous studies.

Acknowledgements

This project has received funding from the European Research Council (ERC) under the European Union's Horizon 2020 research and innovation programme (grant agreement No 950466).

Special thanks are given to the EP team of the ICARE laboratory of the CNRS of Orléans, France and especially to Alfredo Marianacci, Etienne Michaux, Kevin Hecky, Fabiano Perini and Vincent Delbosq.

References

[1]C. Charles and R. Boswell, "Current-free double-layer formation in a high-density helicon discharge," *Applied Physics Letters*, vol. 82, no. 9, pp. 1356–1358, 2003.

[2]O. Batishchev, "Minihelicon plasma thruster," *IEEE Transactions on Plasma Science*, vol. 37, no. 8, pp. 1563–1571, 2009.

[3]K. Takahashi, A. Chiba, A. Komuro, and A. Ando, "Axial momentum lost to a lateral wall of a helicon plasma source," *Physical review letters*, vol. 114, no. 19, p. 195001, 2015.

[4]J. Navarro-Cavallé, M. Wijnen, P. Fajardo, and E. Ahedo, "Experimental characterization of a 1 kw helicon plasma thruster," *Vacuum*, vol. 149, pp. 69–73, 2018.

[5]G. Bethke and D. Miller, "Cyclotron resonance thruster design techniques.," *AIAA Journal*, vol. 4, no. 5, pp. 835–840, 1966.

[6]S. Peterschmitt and D. Packan, "Impact of the microwave coupling structure on an electron-cyclotron resonance thruster," *Journal of Propulsion and Power*, vol. 37, no. 6, pp. 806–815, 2021.

[7]M. R. Inchingolo, M. Merino, and J. Navarro-Cavallé, "Plume characterization of a waveguide ecr thruster," *Journal of Applied Physics*, vol. 133, no. 11, p. 113304, 2023.

[8]F. Cannat, T. Lafleur, J. Jarrige, P. Chabert, P. Elias, and D. Packan, "Optimization of a coaxial electron cyclotron resonance plasma thruster with an analytical model," *Physics of Plasmas*, vol. 22, no. 5, p. 053503, 2015.

[9]T. Vialis, J. Jarrige, A. Aanesland, and D. Packan, "Direct thrust measurement of an electron cyclotron resonance plasma thruster," *Journal of Propulsion and Power*, vol. 34, no. 5, pp. 1323–1333, 2018.

[10]K. Vereen, A. Kimber, J. Correy, D. Olson, H. Martin, and R. Winglee, "Characterization of a cluster of high power helicon thrusters," in *AIAA Propulsion and Energy 2021 Forum*, AIAA 2017-4628, 2017.

[11]K. Vereen, J. Correy, H. Martin, K. Durkee, A. Kullman, S. Fraser, and R. Winglee, "Recent advances in the clustering of high power helicon thrusters," in *AIAA Propulsion and Energy 2019 Forum*, AIAA 2019-3902, 2019.

[12]M. Merino, D. García-Lahuerta, and E. Ahedo, "Plasma acceleration in a magnetic arch," *Plasma Sources Science and Technology*, vol. 32, p. 065005, jun 2023.

[13]C. Boyé, J. Navarro-Cavallé, and M. Merino-Martinez, "Preliminary analysis of the magnetic arch plasma expansion in a cluster of two ECR plasma thrusters," in *10th EUCASS Conference*, (Lausanne, Switzerland, July 9–13), 2023.

[14]M. Inchingolo, J. Navarro-Cavallé, and M. Merino, "Direct thrust measurements of a circular waveguide electron cyclotron resonance thruster," in 37^{th} *International Electric Propulsion Conference*, no. IEPC-2022-338, (Boston, MA, June 19-23), Electric Rocket Propulsion Society, 2022.

[15]R. B. Lobbia and B. E. Beal, "Recommended practice for use of langmuir probes in electric propulsion testing," *Journal of Propulsion and Power*, vol. 33, no. 3, pp. 566–581, 2017.

[16]S. T. Lai and C. Miller, "Retarding potential analyzer: Principles, designs, and space applications," *AIP Advances*, vol. 10, no. 9, p. 095324, 2020.

[17]S. Correyero, J. Jarrige, D. Packan, and E. Ahedo, "Plasma beam characterization along the magnetic nozzle of an ECR thruster," *Plasma Sources Science and Technology*, vol. 28, no. 9, p. 095004, 2019.

[18]A. Sánchez-Villar, F. Boni, V. Désangles, J. Jarrige, D. Packan, E. Ahedo, and M. Merino, "Comparison of a hybrid model and experimental measurements for a dielectric-coated coaxial ECR thruster," *Plasma Sources Science and Technology*, vol. 32, no. 1, p. 014002, 2023.

[19]T. Collard, M. Byrne, S. Hepner, C. Durot, and B. Jorns, "Investigation of detachment in a miniature magnetic nozzle source," in 35^{th} *International Electric Propulsion Conference*, IEPC-2017-361, (Atlanta, GA), Electric Rocket Propulsion Society, Fairview Park, OH, 2017.

[20]S. Mazouffre, "Laser-induced fluorescence diagnostics of the cross-field discharge of Hall thrusters," *Plasma Sources Science and Technology*, vol. 22, p. 013001, nov 2012.